

Formation Mechanism and Nucleation Effect of Ti_2O_3 -TiN Complex Nucleus at Solidification Front of 18Cr Ferritic Stainless Steel



YUYANG HOU and GUOGUANG CHENG

Formation mechanism of Ti_2O_3 -TiN complex nucleus and its nucleation effect on δ -Fe at solidification front of Fe-18Cr ferritic stainless steel was investigated through experimental and theoretical methods. According to the equilibrium calculation, Ti_2O_3 will crystallize in the molten steel before solidification and TiN will not form until the solid phases appear. However, complex nucleus and equiaxed grains exist in the edge of Ti-bearing ingot, where the solidification velocity and temperature gradient are high. Therefore, complex nucleus is indicated to be formed at solidification front and a non-equilibrium solidification model for multi-component alloy was established to investigate the dendrite tip interface phenomenon. The calculation results exhibit an element enrichment at solidification front and explain well with the formation of complex nucleus before solidification. It is also found that there is approximate lattice matching between TiN, and Ti_2O_3 , δ -Fe on the basis of disregistry theory. These results are consistent with the observed complex nucleus and the increased equiaxed zone ratio (EZR) of Ti-bearing ferritic stainless steel.

<https://doi.org/10.1007/s11663-019-01540-0>

© The Minerals, Metals & Materials Society and ASM International 2019

I. INTRODUCTION

FERRITIC stainless steel (FSS), with a content of 11 to 30 mass pct chromium and very little nickel, has been attracting more and more attention for its outstanding characteristics, such as lower thermal expansion coefficient, lower sensitivity to stress corrosion cracking, higher thermal conductivity, when comparing with conventional austenitic stainless steel.^[1,2] In recent years, in view of the hikes in nickel prices and energy saving, FSS, with huge price superiority, has been increasing rapidly in large quantities as a substitute for SUS 304, which occupies the main stainless steel market. Formerly, FSS was subjected to intergranular corrosion (IGC) due to the chromium-depleted region caused by formation of chromium carbonitride in the grain boundary.^[3-9]

Afterwards, IGC was effectively eliminated by reducing the carbon and nitrogen content and introducing stabilizing element Ti, which has an affinity with C and N. Therefore, Ti-bearing FSS gradually occupied the mainstream of the market. Nowadays, the typical shortcomings of the FSS are poor formability and the

occurrence of ridging, which seriously affect the surface quality of the product and restrict the application of FSS.^[10-20]

Many material scientists have concluded that the origin of ridging is strongly related to the columnar structure in the solidification structure of FSS.^[21-31] Therefore, equiaxed grain structure of FSS is desired to be obtained after the solidification process.^[32] Among them, the control of TiN is thought to be the most effective method to improve the equiaxed zone ratio (EZR) of FSS, because of the similarity of lattice parameters between TiN and material matrix.^[33,34] However, to avoid processing problems and poor mechanical properties caused by excessive Ti content, the application of oxide-TiN is proposed through accurate component control.^[35-39] Recently, Ti_2O_3 -TiN was found after solidification of stainless steel,^[40] but few research has been done on the formation mechanism and nucleation effect on δ -Fe.

Typically, the study on the crystallization behavior of TiN and oxide-TiN mainly relies on equilibrium thermodynamic calculations.^[41-43] These studies have shown that TiN is mainly formed during solidification. For equiaxed crystallization, however, it is thought to be necessary to generate TiN at the solidification front to promote a heterogeneous nucleation of δ phase. Additionally, in the actual solidification process, a large amount of TiN and oxide-TiN are found inside the equiaxed grains, and the equiaxed zone ratio is also

YUYANG HOU and GUOGUANG CHENG are with the State Key Laboratory of Advanced Metallurgy, University of Science and Technology Beijing, Beijing 100083, China. Contact e-mail: chengguoguang@metall.ustb.edu.cn

Manuscript submitted September 23, 2018.

Article published online February 15, 2019.

improved due to the presence of TiN and oxide-TiN. However, few reports focus on the formation mechanism of TiN and oxide-TiN at the solidification front.

Due to differences in elemental solubility between the solid and liquid phases, the solute redistribution occurs at the interface, which phenomenon cannot be calculated by equilibrium thermodynamics. In addition, under certain conditions of solidification velocity and temperature gradient, the solute concentration, solidus, liquidus and formation temperature of TiN at the solidification front will change significantly.

In this work, the formation mechanism and characteristic of Ti_2O_3 -TiN complex nucleus at the solidification front in 18Cr FSS were investigated during non-equilibrium solidification, which have been seldom studied so far.

II. EXPERIMENTAL AND MODELING

A. Experimental Procedure

Two ingots of approximately 1.0 kg mass were prepared in a vacuum induction furnace. Ingot A is a control sample and Ingot B is a Ti-bearing experimental sample. To avoid the oxygen source from raw materials, during the experiment, the basic alloys with composition of Fe-18 mass pct Cr-0.32 mass pct Si and Fe-18 mass pct Cr-0.30 mass pct Si-0.22 mass pct Ti were first remelted in MgO crucible for Ingot A and Ingot B, respectively. In addition, at the beginning of the experiment, the vacuum in the induction furnace was pumped to 10Pa, and then high-purity argon (volume fraction > 99.999 pct) was introduced to the furnace. The above operation was repeated by three times, and the total pressure was finally maintained at about 10 Pa to reduce the partial pressure of oxygen in the atmosphere as much as possible. Temperature of molten steel was measured by Raytek Marathon MR1SB infrared thermometer. When the melt temperature reached 1600 °C, the molten steel was held for 5 minutes, after which the molten steel was cast into mold at 1570 ± 15 °C. The ingots were removed from the mold 5 minutes later and quenched to the room temperature in water.

The shape of these ingots is truncated cone with the height of 80 mm, the bottom diameter of 40mm and the top diameter of 50 mm. The ingots were cut into two parts vertically through the centerline. One part was etched by aqua regia solution ($HCl:HNO_3 = 3:1$) to reveal the as-cast structure. In another part, a metallographic sample was cut in the middle of these ingots from the side to the center. The ingot outline dimensions and the sampling method are shown in Figure 1. The alloying element contents in the two ingots were measured by the alkali fusion acid dissolution method. The chemical compositions are shown in Table I.

The morphology and distribution of the complex nucleus were observed by Leica DM4M optical microscope (OM). Then characteristic and composition were analyzed by application of FEI Quanta SEM with an EDS X-ray analyzer. In addition, micro-Raman

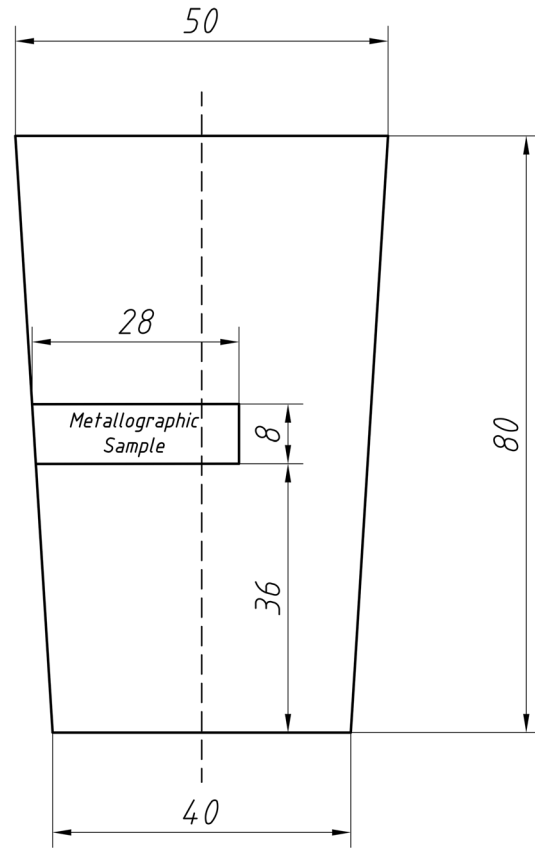


Fig. 1—Ingot outline dimensions and the sampling method.

Table I. Composition of the Two Ingots (Mass Percentage)

Ingot	Cr	Ti	C	N	O	Si
A	17.85	0.001	0.0065	0.0098	0.0130	0.33
B	17.98	0.200	0.0066	0.0110	0.0018	0.27

spectrometer was applied to analyze the oxide core in the complex nucleus on the platform of HORIBA LabRAM HR Evolution.

B. Solute Distribution During Non-equilibrium Solidification Process

In an actual solidification process, elements will be enriched at the front of the solid-liquid interface due to the segregation phenomenon, which has a great influence on the precipitation behavior of FSS. To reveal the solute enrichment at the solidification front during non-equilibrium solidification process, the solute distribution of component i can be obtained by Ivantsov's solution, as expressed by Eq. [1]^[44]:

$$C_{1,i,z}^* = C_{0i} + (C_{li}^* - C_{0i}) \frac{E_1[P_c(2z + R)/R]}{E_1[P_c]}, \quad [1]$$

where C_{li}^* is the interface concentration of element i ; C_{0i} is the initial composition of element i ; P_c is the solutal Peclet number; R is the tip radius of a dendrite

growing at steady state; E_1 is the integral exponential function; z is the distance in the liquid from the tip of the dendrite parallel to the dendrite axis. Under non-equilibrium solidification conditions, P_c , R , and C_{li}^* are related to the velocity of solidification interface between solid and liquid, which can be obtained by non-equilibrium solidification model. This multi-component model was established based on the dendritic growth kinetics proposed by Kurz–Giovannola–Trivedi.^[45] The modeling details have been given in a previous work.^[46]

III. RESULTS

A. Solidification Structure

Figure 2 shows the solidification structures of these ingots, from which it can be seen that the EZR of the Ingot B reached almost up to 100 pct compared with Ingot A. The solidification parameters in the CET

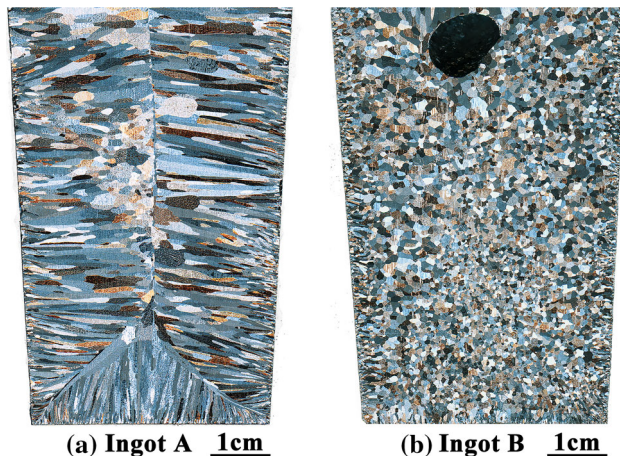


Fig. 2—The solidification structure of the 18Cr FSS. (a) Ingot A; (b) Ingot B.

position can be obtained using the same method as the previous work.^[46] The temperature gradient can be obtained as 13 K/mm, and the interface velocity to be 400 $\mu\text{m/s}$. Under such solidification conditions, the typical solidification structure is supposed to be mainly composed of columnar grains^[47,48] as Ingot A shown in Figure 2(a).

The major inclusions in Ingot A are spherical SiO_2 with an average diameter of 1.48 μm , of which the typical morphology and composition are shown in Figure 3. While different from Ingot A, the major inclusions in Ingot B are mainly Ti-bearing complex nuclei. This phenomenon demonstrates that heterogeneous nucleation might have occurred in Ingot B. Therefore, a series of detailed investigation were conducted on Ingot B.

B. The Morphology and Distribution of Complex Nucleus

The complex nuclei, observed by optical microscope(OM) at magnification of $\times 1000$, are shown in Figure 4. These inclusions were recognized to be orange color when performing bright field contrast in external light mode. Additionally, a black core exists in each orange inclusions. According to the following EDS analysis, the orange part was identified to be TiN and the black core to be titanium oxide. Both of them constitute complex nucleus together, of which the morphology is regular polygon and having a uniform distribution.

More detailed morphology of these typical complex nuclei shown in Figure 5 were observed by SEM analysis with backscattered electron mode. Similar to the optical microscope results, it was shown that a black core exists in all the complex nuclei. The characteristic size of the most complex nuclei is between 2 and 4 μm . In addition, not all the black cores are located exactly in the center of these inclusions. Sometimes the black core locates in the center as shown in Figures 5(a) through (f), and sometimes in the corner shown in Figures 5(g)

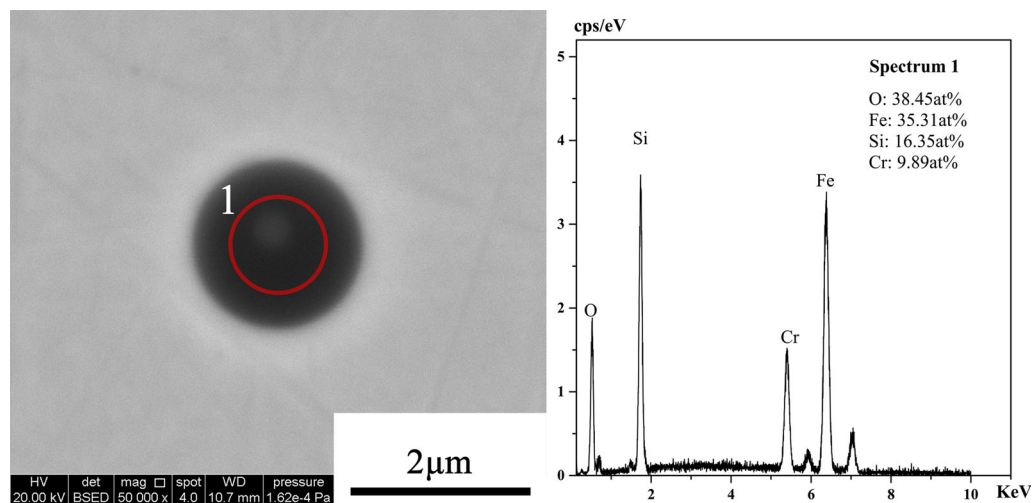


Fig. 3—Typical morphology and composition of SiO_2 in Ingot A.

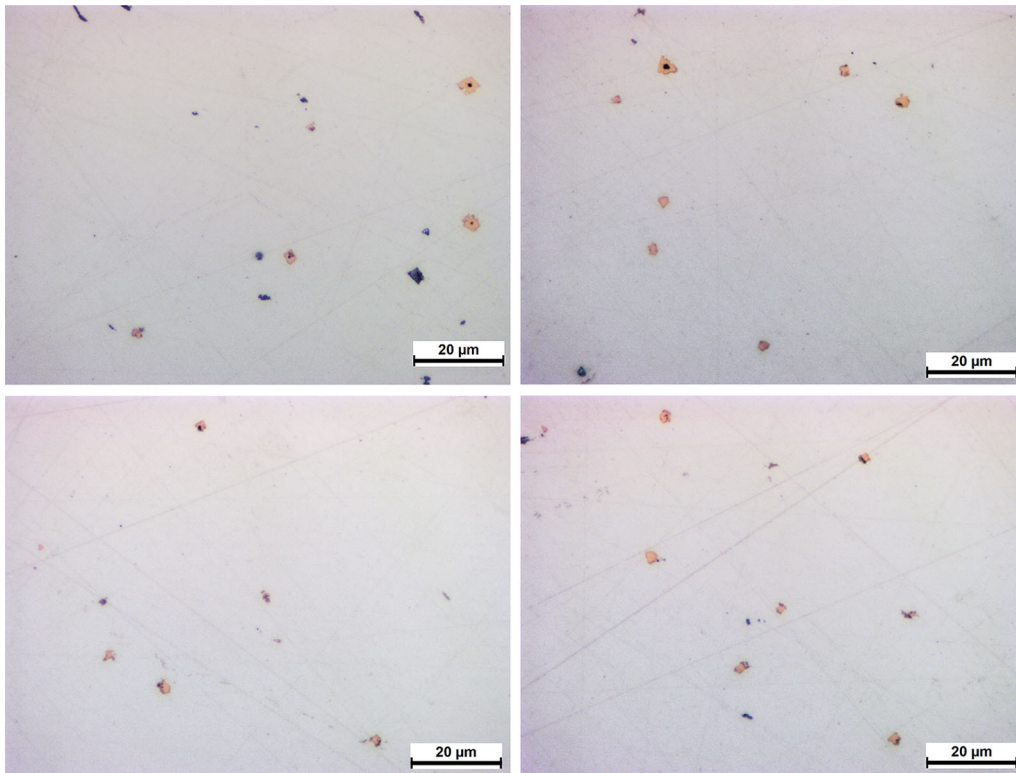


Fig. 4—The complex nuclei observed by OM with $\times 1000$ magnification.

through (i). Moreover, the size of black core differed in different complex nuclei, sometimes the size very small (hundreds of nanometers).

C. The Characteristic and Composition of Complex Nucleus

The typical characteristic and component of these complex nuclei further revealed by EDS analysis are shown in Figure 6. As can be seen from Figure 6, the black cores of these complex nuclei are identified to be titanium oxide whether located in the center or in the corner. The gray part surrounding the black core is TiN.

In addition, map scanning was applied to reveal the element distribution of complex nucleus. The result is shown in Figure 7. Map scanning field of view is shown in Figure 7(f), the element distributions of Ti, O, N, Fe, Cr are shown in Figures 7(a) through (e), respectively. The brightness of the color represents the content of the corresponding element. It can be seen that the Ti element is uniformly distributed in the complex nucleus, which can be clearly distinguished from the surrounding Fe and Cr-rich matrix. What is more, the enrichment of oxygen is mainly concentrated in black core of complex nucleus, whereas the element N is concentrated in the other parts of complex nucleus than the black core. The black part can be identified to be titanium oxide, the dark gray part (orange part in the OM results) to be TiN according to the analysis of EDS and map scanning.

There are many forms of titanium oxide with different lattice structures, such as TiO, TiO₂, Ti₂O₃ and Ti₃O₅.^[31,49,50] Each of them has different lattice matching with TiN. Although it can be identified that the complex nucleus is composed of titanium oxide and TiN according to the EDS results, it is necessary to figure out the specific form of titanium oxide.

First of all, the composition of 200 oxide cores in complex nuclei were statistically analyzed to reveal the O/Ti atomic ratio. However, there sometimes exist N element in the EDS results as shown in Figure 6. This phenomenon may be attributed to the spatial resolution of the SEM-EDS. Since the oxide size in the complex nucleus is generally small, mostly 1 micron and below, usually smaller than the beam spot size of the SEM-EDS. External TiN of complex nucleus may have an influence on the EDS results. Therefore, when analyzing the O/Ti ratio, TiN is removed by stoichiometric ratio in data processing. The result is shown in Figure 8. The abscissa represents the atomic percentage of the data-processed Ti element in these oxide cores, and the ordinate is the O element. The blue balls represent the experimental data, and the red dotted line represents the ideal O/Ti atomic ratio of Ti₂O₃. It can be seen from the figure that the O/Ti atomic ratio of the oxide cores in the complex nucleus are located around that of Ti₂O₃, indicating that the titanium oxide is Ti₂O₃ in the complex nucleus. In addition, the smaller the size of oxide core is, the less content of Ti and O will be, as shown in the lower-left corner in Figure 8. These data

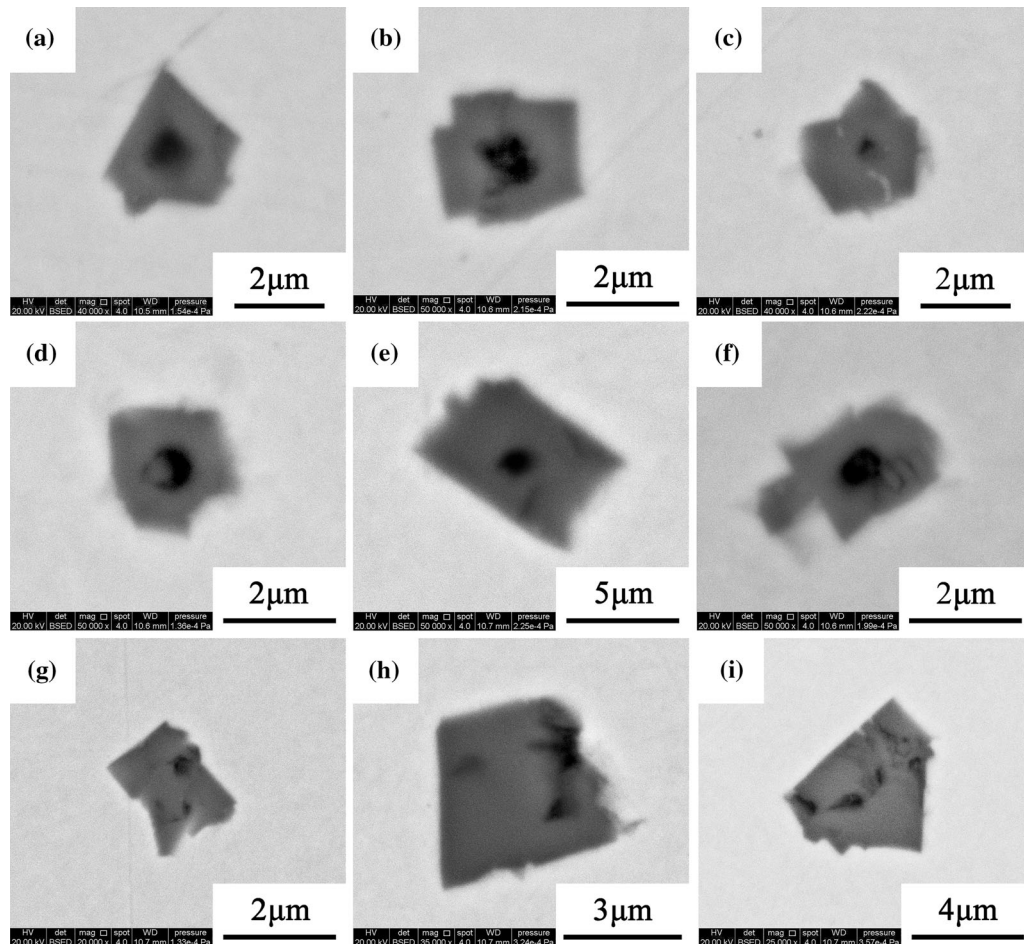


Fig. 5—Typical morphology of complex nuclei observed by SEM. (a) through (f) Oxide core locates in the center of complex nucleus; (g) through (i) Oxide core locates in the corner of complex nucleus.

are also more dispersed in this area. Although the statistical results can explain the form of titanium oxide to a certain extent, further research is necessary to confirm the exact form of the oxide core. Therefore, the Raman spectroscopy analysis was applied to the oxide identification.

Figure 9(a) shows the Raman spectra of oxide core in complex nucleus, of which the SEM image and laser point are shown in Figure 9(b). The Raman spectra of Ti_2O_3 ^[51,52] and TiN ^[53] are shown in Figures 9(c) and (d), respectively. The spot size of the micro-Raman spectrometer system was about $2\ \mu m$.^[54] However, the size of the oxide core is small. To obtain reliable results, a complex nucleus with a larger oxide core is selected for Raman test as shown in Figure 9(b), and the influence of external TiN is hoped to be avoided as much as possible.

The feature peaks of Ti_2O_3 and TiN are represented by triangle and diamond symbols, respectively. By comparison, it can be found in the Raman spectra that the feature peaks of the oxide core coincide with Ti_2O_3 centered at ~ 203 , ~ 247 , $\sim 291 \sim 335$, ~ 423 and $\sim 550\ cm^{-1}$ and with TiN centered at ~ 203 , ~ 335 and $\sim 550\ cm^{-1}$. It can be concluded from the Raman results that the oxide core is composed of Ti_2O_3 and very little TiN . TiN may be derived from external influences. Besides, many studies have also shown that the solubility of N

increases when the TiO_x content in the slag arises,^[55–58] the TiN may have already present in the oxide core before solidification. Accordingly, there will be a new mechanism for the formation of complex nucleus besides interface theory such as lattice disregistry and wetting angle.^[33,49] However, it is difficult to validate the nitrogen solubility in Ti_2O_3 during solidification and beyond the scope of this article. It is reported that Ti_3O_5 is a thermodynamically more stable phase under melting stage, but the oxide core is identified to be Ti_2O_3 in this work, the formation mechanism will be discussed later.

In this work, the complex nuclei were found to be uniformly distributed in the experimental sample and numerous in quantity. According to the research by Bramfit,^[33] Villafuerte *et al.*,^[59] TiN is very effective for promoting the heterogeneous nucleation of ferrite.

Therefore, TiN in the complex nucleus might be the directive reason for the EZR improvement of the ingot B. However, the supersaturation required for the formation of TiN leads to an excessive amount of Ti , which cause the aggregation of TiN and the formation of harmful inclusions.^[31,60] It is worth noting that the content of Ti in this work is at a low level and Ti_2O_3 exist in almost all the complex nucleus. It is important to find out whether the Ti_2O_3 could come into formation and promote the formation of TiN afterwards.

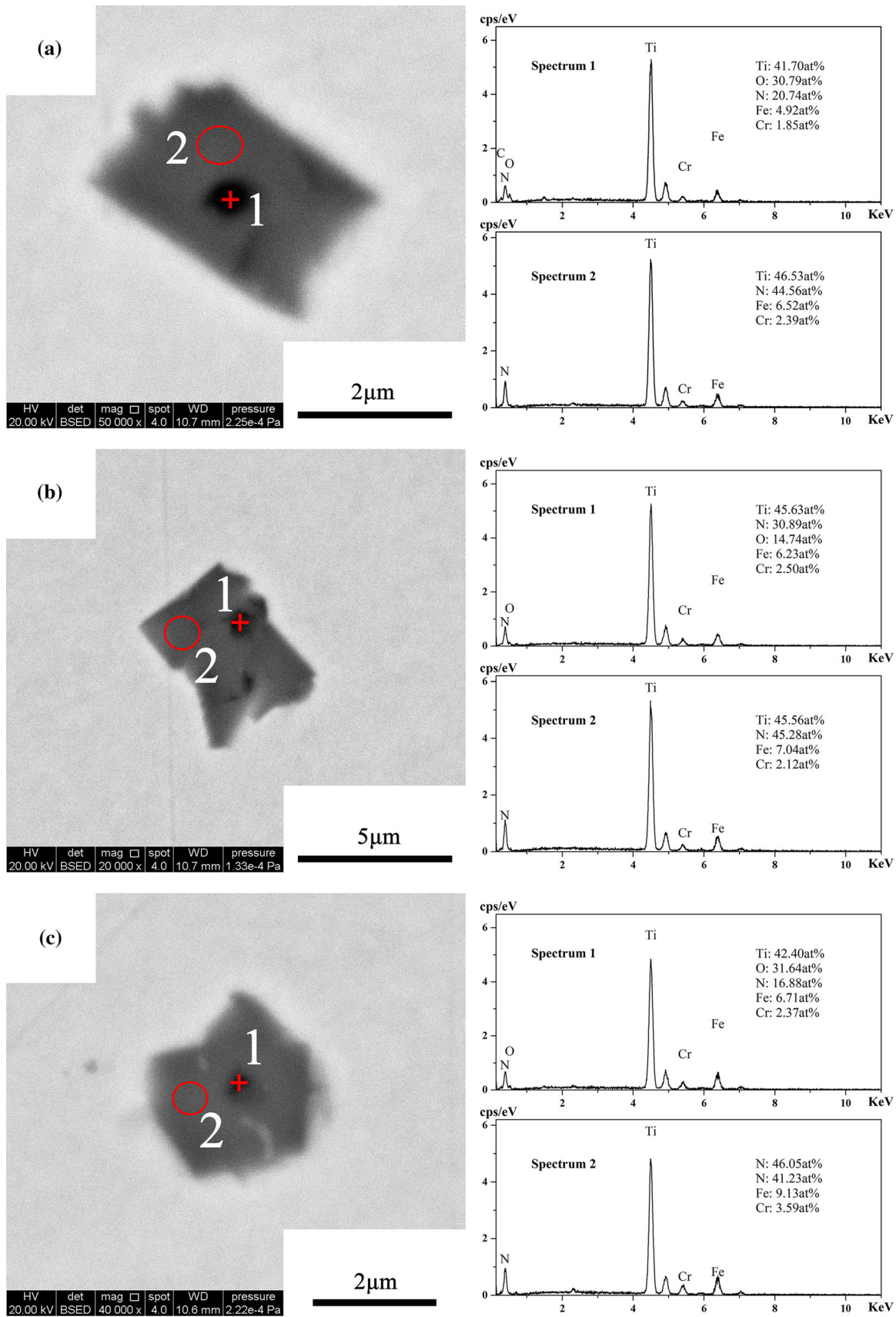


Fig. 6—Typical composition of complex nuclei in Ingot B. (a) Big oxide core in the center; (b) Small oxide core in the corner; (c) Small oxide core in the center.

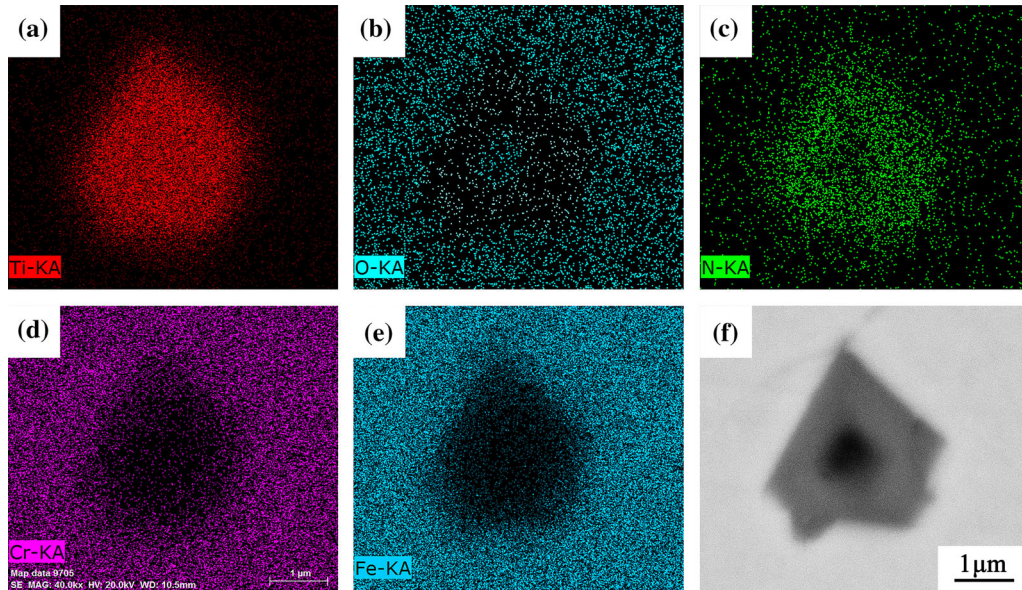


Fig. 7—Element map scanning of complex nucleus in the matrix by EDS. (a) Ti; (b) O; (c) N; (d) Cr; (e) Fe; (f) SEM image.

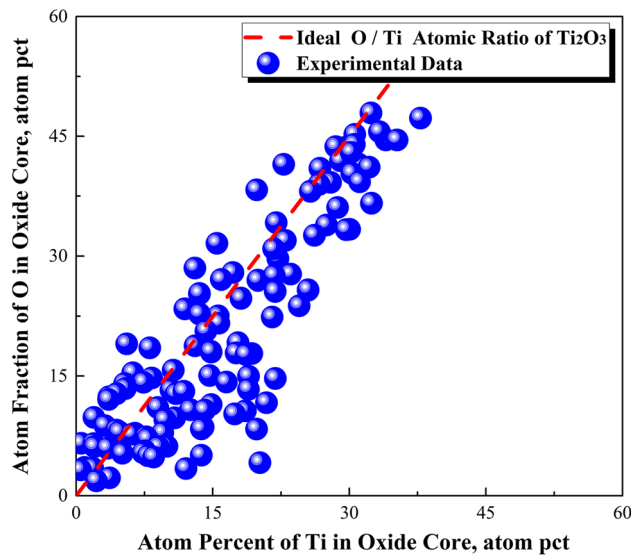


Fig. 8—Statistical result of oxide cores in complex nuclei. Blue ball represents for the experimental data and red-dashed line for the ideal O/Ti atomic ratio of Ti_2O_3 (Color figure online).

Therefore, the formation mechanism of complex nucleus and nucleation effect between titanium oxide and TiN at the solidification front is discussed in the following part.

IV. DISCUSSION

A. Equilibrium Phase Diagram of Fe-18Cr FSS Under Different Ti Content

To reveal the formation mechanism of complex nucleus, the equilibrium phase of Ti-bearing Fe-18Cr ferritic stainless steel was carried out under different Ti content on the basis of 18 mass pct Cr-0.007 mass pct C-0.011 mass pct N with help of FactSage, which is a

commercial thermochemical software with an abundant database. FactSage is based on the calculation of Gibbs energies of possible existing phases. By minimizing this Gibbs energy, the most stable phase composition of the system is calculated. The result is shown in Figure 10. The content range of Ti is from 0 to 1.0 mass pct, and the temperature range from 1200 to 1600 °C. As shown in Figure 10, line AB, CD, IJK, and EFGH represent the liquidus, the solidus, formation temperature for titanium oxide, and for TiN, respectively. Line JLMN represent phase boundary between Ti_3O_5 and Ti_2O_3 . With the increase of Ti content, titanium oxide transforms from Ti_3O_5 into Ti_2O_3 . The critical transformation content of Ti decreases with the decrease of temperature. The dot-dashed line represents the content of Ti in this work and it is easier to form Ti_2O_3 during solidification.

The following information can be obtained from Figure 10. First, titanium oxide will come into formation in the liquid phase when Ti content exceed 0.044 mass pct (point I). Second, the formation temperature of TiN is gradually increasing with the increase of Ti content. TiN will form after solidification, when the Ti content locates within the range from 0 to 0.04 mass pct (line EF), where TiN has no nucleation effect on δ -Fe under this circumstance. Third, TiN will come into being during solidification, when the Ti content locates within the range from 0.04 to 0.48 mass pct (line FG). In this case, TiN will promote the nucleation of FSS during solidification effectively. What is more, TiN will come into being before solidification, when the Ti content exceeds 0.48 mass pct (line GH), where the TiN is easy to form large size inclusions probably, which should be avoided. In the solidification process of Ingot B represented by dot-dashed line, Ti_3O_5 was first formed at 1570 °C and immediately converted to Ti_2O_3 at 1565 °C. TiN formed at 1500 °C between liquidus (1505 °C) and solidus (1492 °C).

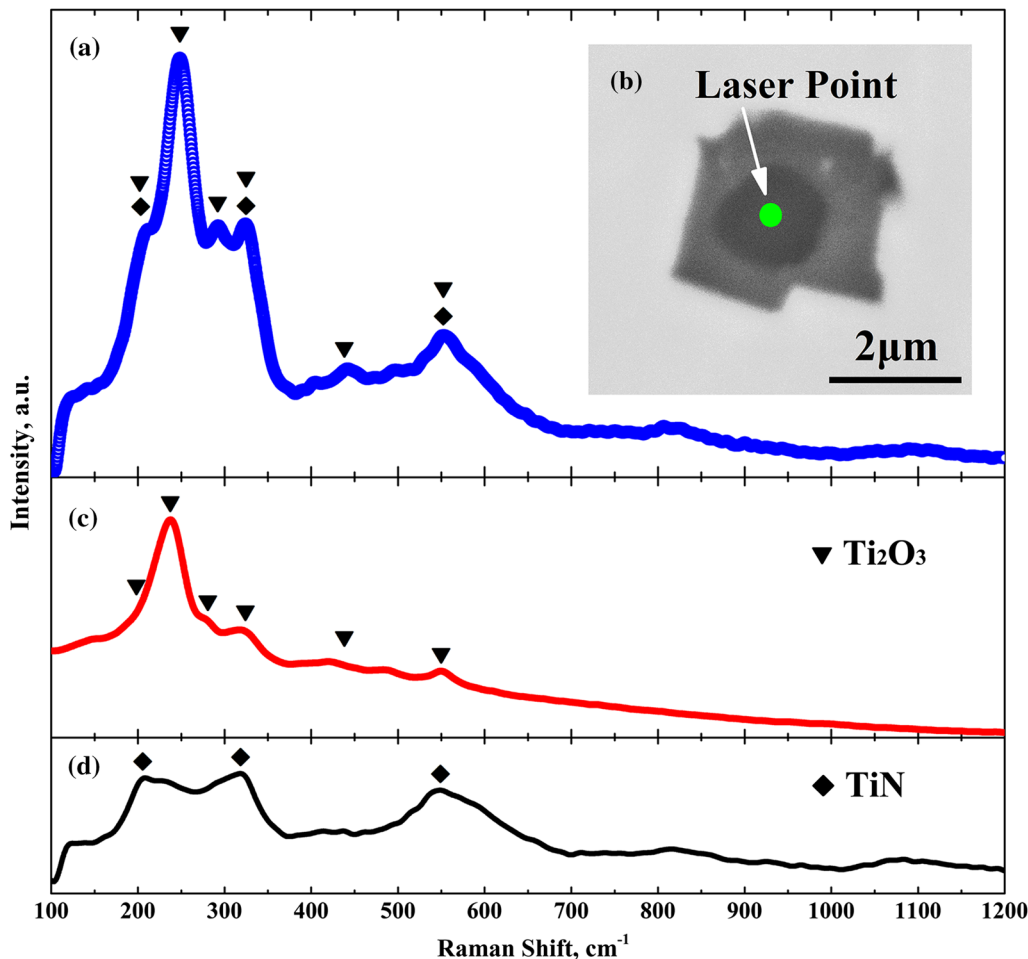


Fig. 9—The Raman spectroscopy result of oxide cores in complex nuclei. (a) Raman spectrum with feature peaks of oxide core in complex nucleus; (b) The complex nucleus morphology for testing and the corresponding laser point; (c) Raman spectrum with feature peaks of Ti_2O_3 ; (d) Raman spectrum with feature peaks of TiN. The feature peaks of Ti_2O_3 and TiN are represented by triangle and diamond symbols, respectively.

It can be seen from the analysis in Section III that the inclusions in Ingot B are mainly Ti_2O_3 –TiN complex nuclei. During solidification, the solute redistribution exists at the solid/liquid interface and element diffusion differs between solid and liquid phase. And the solute distribution during solidification can be described by Scheil–Gulliver model. In this work, the formation mechanism of complex nucleus during solidification was also carried out by Scheil–Gulliver model. The calculated result is shown in Figure 11.

By calculating the Scheil solidification process of Fe-18Cr steel, it can be found that there are three important precipitate phases, which are Ti_2O_3 , TiN and TiC. It can be seen from the calculation result that Ti_2O_3 will come into being when the temperature reach 1565 °C and TiN and TiC begin to generate at 1500°C just below the liquidus(1505 °C). The content of TiN increased rapidly to a certain value the moment it is generated. As for TiC, the content increased slowly at the beginning of solidification but rapidly at the end. Finally, the solidification comes to an end at solidus(1337 °C). In the solidification interval between 1505 and 1337 °C, Ti_2O_3 increases slightly in the beginning

and keeps a lower content relative to Ti(C, N), which correspond to the small size of titanium oxide observed in the OM and SEM.

Scheil model assumes that no diffusion occurs in solid phases and infinitely fast diffusion occurs in the liquid phases.^[61,62] Such assumptions generally exist in a region with little amount of liquid phases, therefore, the Scheil model is often used to predict the precipitation characteristics between primary or secondary dendrites, where behind the dendrite tip or solidification front. Contradictory to the Scheil-cooling FactSage predictions, TiC was not observed in complex nucleus. One possible reason may be that the precipitation of TiC is slow. Another reason is that TiN in the complex nucleus might form before solidification rather than during solidification. It is necessary to discuss the formation possibility of complex nucleus at the solidification front.

Additionally, although TiN will be theoretically generated, the supersaturation required for TiN formation is too high to generate homogeneously. However, a large number of uniformly distributed complex nucleus, composed of TiN and titanium oxide, appeared in the ingot under high cooling rate in this work, indicating

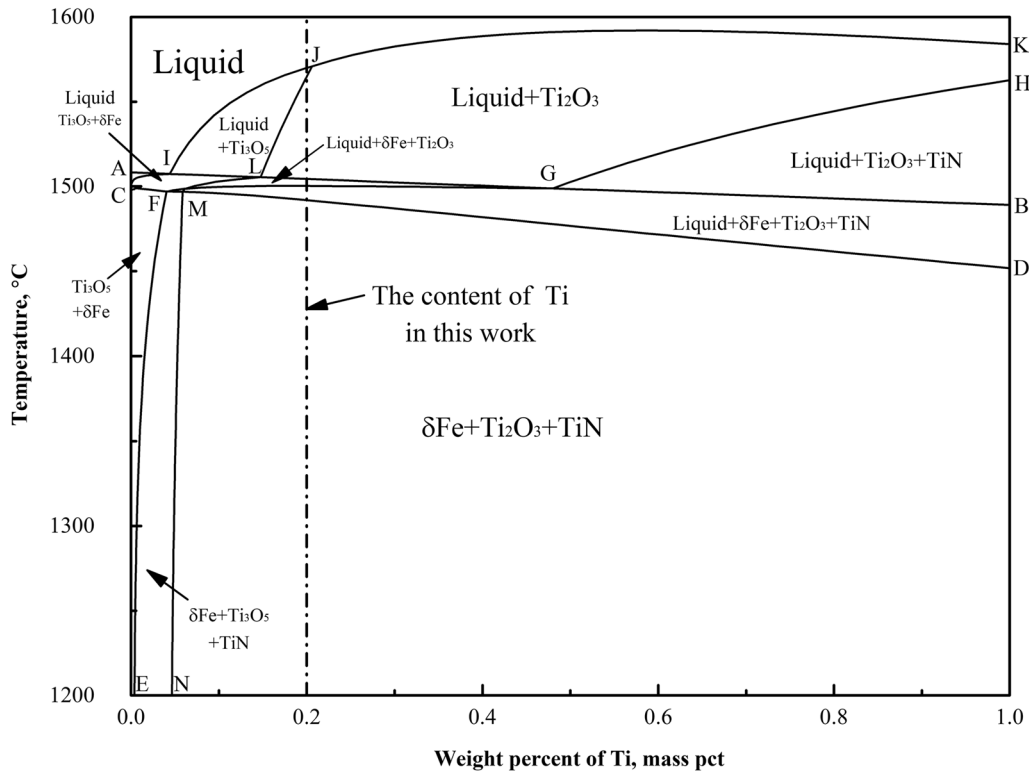


Fig. 10—Ti-Temperature phase diagram of 18Cr FSS. The solid and dot-dashed line represents the phase boundary and Ti content in this work.

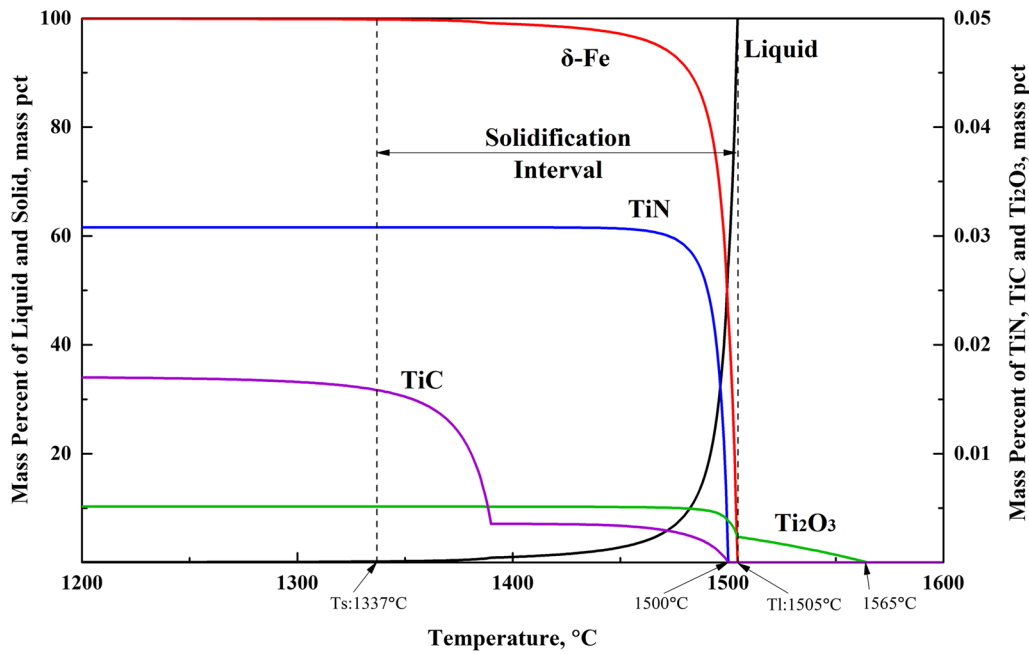


Fig. 11—Scheil solidification process analysis of 18Cr FSS. Left Y-axis represents Liquid and Solid, rescaled right Y-axis represents TiN and TiC.

that TiN will be easily formed together with Ti_2O_3 . If the formation of TiN is promoted by the existing Ti_2O_3 , the nucleation of δ -Fe will further be promoted by TiN.

Finally, the EZR of FSS will be easily increased. The nucleation effect of Ti_2O_3 on TiN will be discussed in Section IV.C.

Table II. The List of Parameters Used in the Multi-component KGT Model

Parameter	Unit	Cr	Ti	Si	C	N	O
$C_{0,i}$	mass pct	18	0.2	0.27	0.007	0.011	0.0018
m_i	mass pct/K	-0.30	-19.27	-1.62	-98.17	-69.93	40
k_i	—	0.99	0.34	0.96	0.17	0.28	0.065
$D_{0,i}$ ^[37]	m ² /s	2.67×10^{-7}	1.81×10^{-7}	2.40×10^{-8}	1.43×10^{-7}	1.43×10^{-7}	1.2×10^{-8}
Q_i ^[37]	J/mol	6.69×10^4	4.77×10^4	1.72×10^4	4.69×10^4	4.69×10^4	in melt ^[63]

Where m_i is the liquidus slope of element i ; k_i is the equilibrium partition coefficient of element i ; $D_{0,i}$ is the liquid-phase diffusion constant of component i ; Q_i is the activation energy.

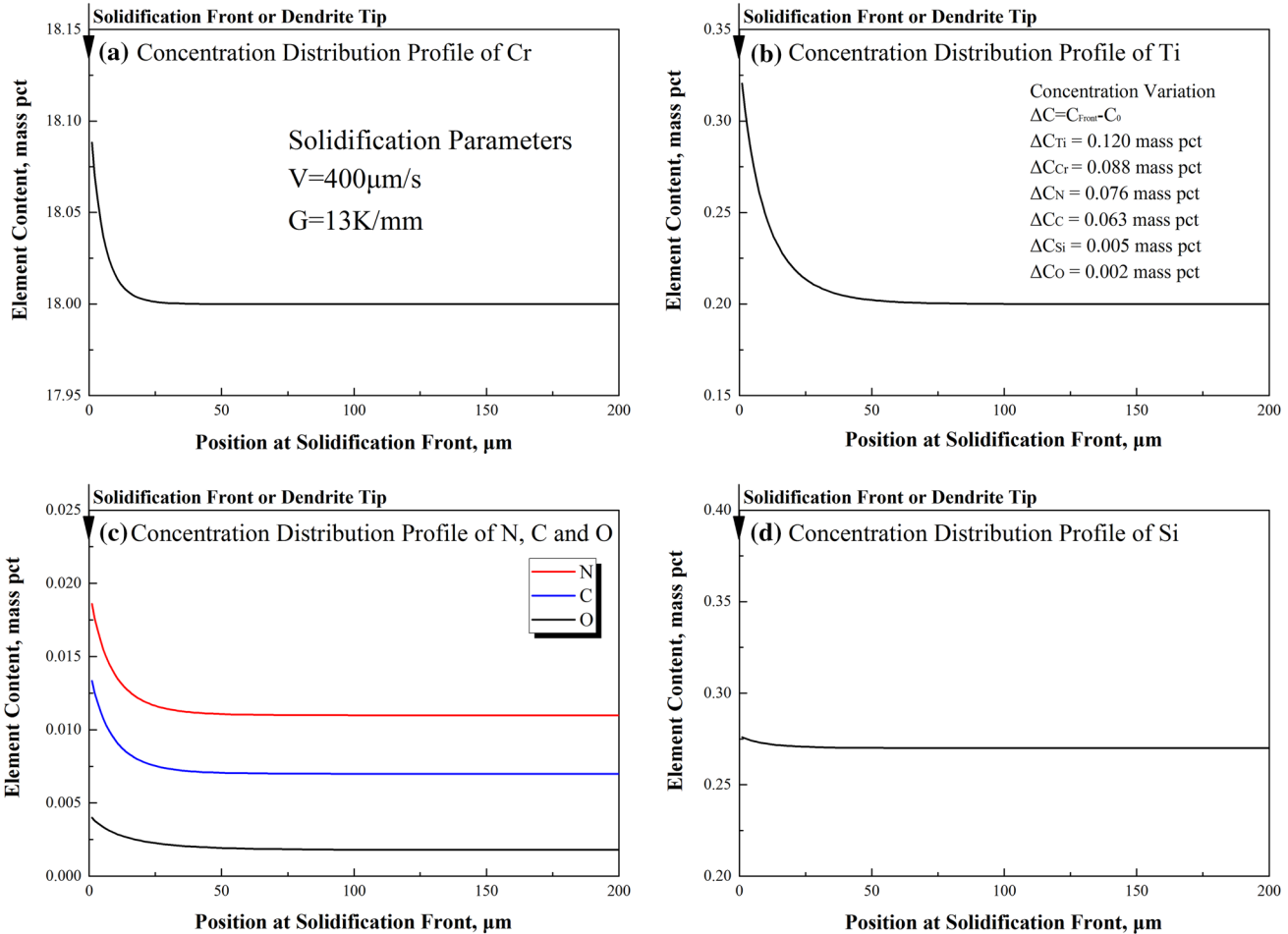


Fig. 12—Distribution of Cr, Ti, C, N, O and Si at the dendrite tip. (a) Cr, (b) Ti, (c) N, C and O, (d) Si (Color figure online).

For equiaxed crystallization, it is thought to be necessary to generate TiN which is thought to be a heterogeneous nucleus of δ phase at the solidification front above liquidus. Therefore, the formation mechanism of complex nucleus at the solidification front will be discussed by the non-equilibrium solidification model.

B. The Formation Mechanism of Complex Nucleus at the Solidification Front

In a previous work,^[46] the dendritic growth characteristics of Nb-bearing Fe-20Cr FSS during non-equilibrium solidification process were carried out by a multi-component KGT model and successfully

predicted the solidification structure. However, whether a complex nucleus can be formed at the solidification front in a Ti-bearing FSS deserves further discussion. Therefore, in this work, the formation mechanism was discussed combined with the non-equilibrium model.

The data used in this work shown in Table II were first obtained through thermodynamic calculation. Before calculation, growth velocity and temperature gradient should be determined. As mentioned in Section III.A, the growth velocity is 400 $\mu\text{m/s}$ and the temperature gradient is 13 K/mm. The initial solute contents were $w[\text{Cr}] = 18$ mass pct, $w[\text{Ti}] = 0.2$ mass pct, $w[\text{Si}] = 0.27$ mass pct, $w[\text{C}] = 0.007$ mass pct and $w[\text{N}] = 0.011$ mass pct. After

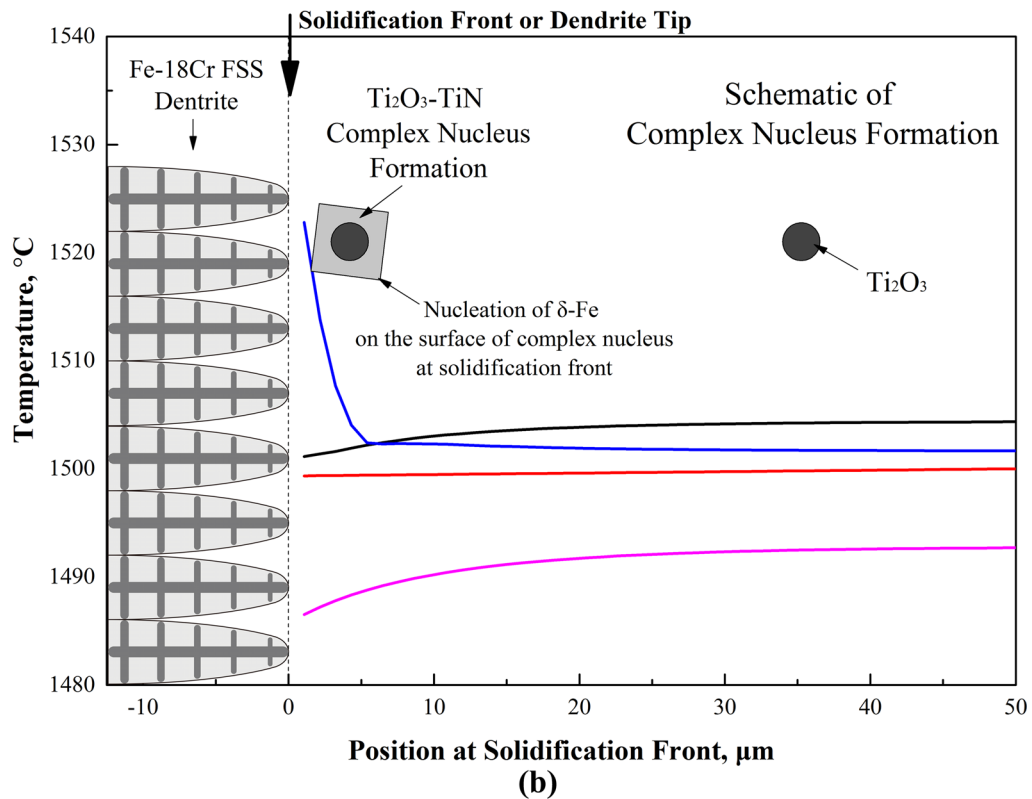
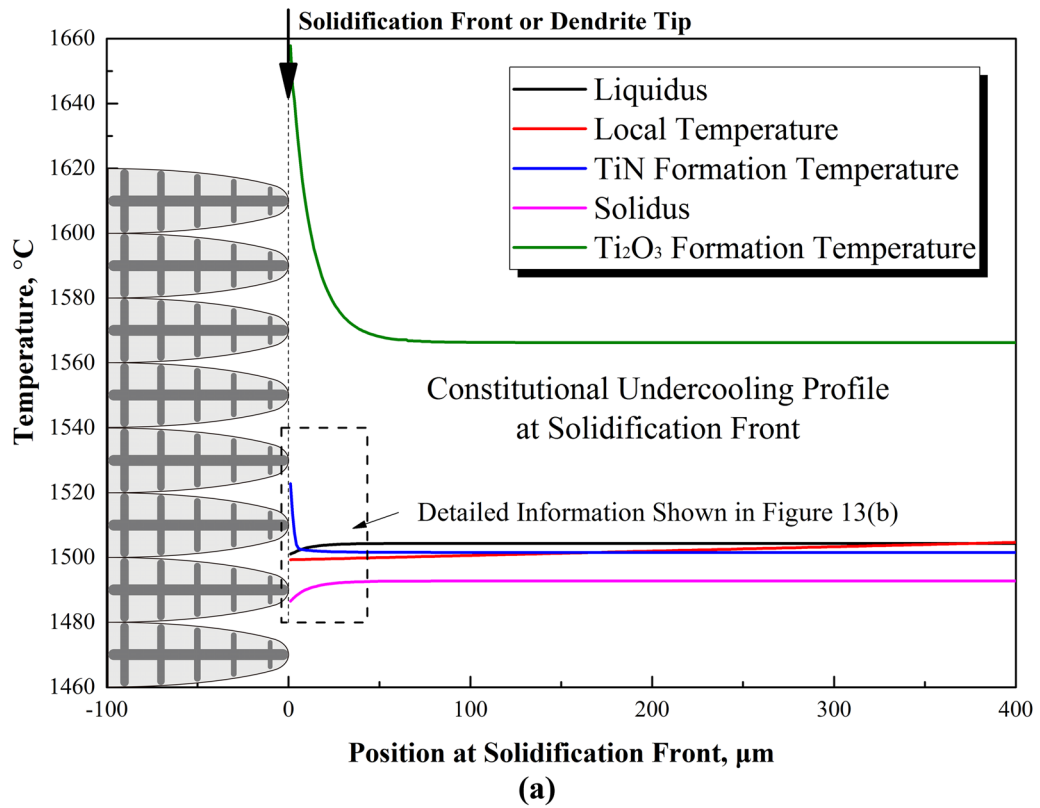


Fig. 13—Schematics of constitutional undercooling and TiN formation temperature ahead at the solidification front. (a) Constitutional undercooling profile, (b) Schematic of complex nucleus formation (Color figure online).

Table III. Lattice Parameters of the Corresponding Material in Steel

Substance	Lattice Structure	a0 at 25 °C /nm	a0 at 1500 °C /nm
δ -Fe	BCC-type	—	0.29396
Ti ₂ O ₃	corundum-type	—	0.51251
TiN	NaCl-type B1	0.42419	0.43055

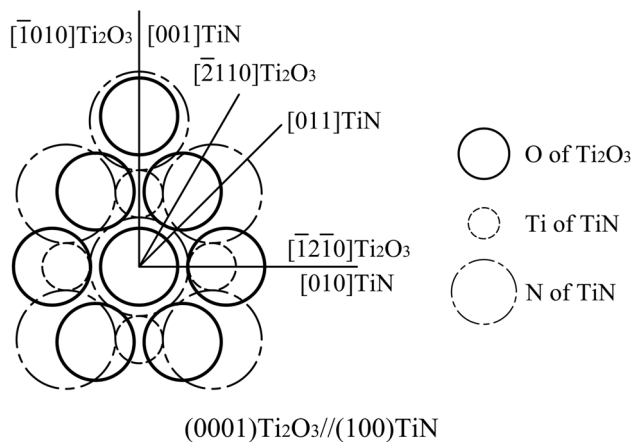


Fig. 14—The orientation relationship between Ti₂O₃ and TiN.

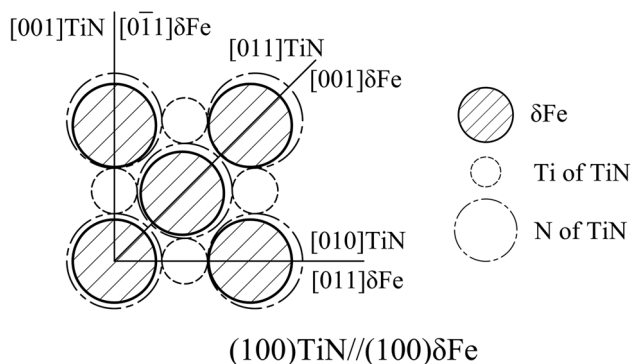


Fig. 15—The orientation relationship between δ Fe and TiN.

dendritic kinetic analysis, solute concentration distribution at the solidification front for component *i* can be obtained.

For Ti-bearing Ingot B, the solute concentration distribution profiles of element Cr, Ti, Si, C, N and O in the liquid phase at solidification front are shown in Figures 12(a) through (d).

Figure 12 shows that the solute enrichment phenomenon exists in the liquid phase within 50 μm ahead of the dendrite tip during solidification. As the element content at the solidification front changes, the liquidus, solidus, TiN and Ti₂O₃ formation temperatures are bound to change correspondingly. These changes were analyzed by FactSage. The constitutional undercooling schematic ahead of the solidification front of the

Ti-bearing Ingot B is shown in Figure 13(a). The detail at the solidification front within 50 μm is enlarged as shown in Figure 13(b).

As can be seen from Figure 13(a), constitutional undercooling exists in the distance range from 0 to 360 μm . Due to the change of concentration distribution at the solidification front, the solidus and liquidus are decreased, but the TiN and Ti₂O₃ formation temperature is increased. The local temperature does not exceed the formation temperature of TiN until the distance beyond 173 μm . It is noteworthy that the formation potential of TiN is greater than that of δ -Fe within 6 μm because of the result that formation temperature of TiN is higher than the liquidus, which is different from the thermodynamic calculation results as shown in Figures 10 and 11.

Therefore, TiN can be precipitated at the solidification front, resulting in nucleation of δ -Fe. And TiN will not further cluster to become inclusions when the position is 6 μm beyond solidification front. However, experimental results show that most of TiN is combined with Ti₂O₃, which has been existed before the formation of solid. Therefore, the possibility of TiN generated on the surface of Ti₂O₃ will be discussed through disregistry theory in the following section.

C. The Nucleation Effect Between Titanium Oxide and TiN

Bramfitt put forward the disregistry concept to measure the effectiveness of heterogeneous nucleation. The effective heterogeneous nucleation can reduce the nucleation energy of δ -Fe in the solidification process, thereby reducing the nucleation undercooling and the required supersaturation of nucleated solid.

With the help of the disregistry calculations, Bramfitt,^[33] Park *et al.*,^[64] Cheng *et al.*,^[29] has reported the effective nucleation of TiN on δ -Fe. However, few people have discussed the nucleation effect of Ti₂O₃ on TiN in Fe-18Cr ferritic stainless steel. The lattice disregistry between TiN and Ti₂O₃ together with δ -Fe was discussed to investigate the nucleation effect of Ti₂O₃ on TiN and of complex nucleus on δ -Fe.

The lattice parameters of the relevant material are given in Table III.^[65] The orientation relationship between Ti₂O₃ and TiN, is shown in Figure 14. The orientation relationship between δ -Fe and TiN is shown in Figure 15.

According to the disregistry calculation model proposed by Bramfitt, the disregistry between TiN and Ti₂O₃ is 13.61 and that between TiN and δ-Fe is 3.57. According to the disregistry theory, it can be concluded that there has approximate lattice matching between TiN, and Ti₂O₃, δ-Fe.

It can be concluded that Ti₂O₃, formed in the liquid steel during solidification, will further promote the formation of TiN to create a complex nucleus at the solidification front. The heterogeneous nucleation of δ-Fe will be promoted once the complex nucleus is formed. As a result, the growth of the columnar grains is suppressed, and the equiaxed grain ratio will be increased.

V. CONCLUSION

In this paper, the formation mechanism and nucleation effect of Ti₂O₃-TiN complex nucleus during solidification process of Fe-18Cr ferritic stainless steel was studied, and the following conclusions were obtained.

1. When Ti was added, the inclusions in the FSS changed from SiO₂ to Ti₂O₃-TiN complex nucleus. The EZR increased almost to 100 pct in Ingot B compared with Ingot A.
2. Although Ti₂O₃ can be formed in the high-temperature liquid phase region during solidification, the formation of TiN lags behind that of solid phase whether based on the equilibrium or Scheil-cooling calculation results. Therefore, the component variation at the dendritic tip during non-equilibrium solidification should be taken into account when discussing the formation mechanism of TiN.
3. The formation of TiN at solidification front was discussed with the help of multi-component dendritic growth model during non-equilibrium solidification. The results show that formation temperature of TiN is larger than the liquidus within 6 μm ahead of the solidification front. This result indicates that TiN will form earlier than the solid phase, which is different from the equilibrium thermodynamic calculation.
4. The nucleation effect of Ti₂O₃ on TiN was discussed on the basis of disregistry theory. The results show that there is approximate lattice matching between TiN, and Ti₂O₃, δ-Fe, indicating that the existing Ti₂O₃ will promote the formation of TiN both prior to (ahead of the dendrite front) and during solidification. Additionally, the heterogeneous nucleation of δ-Fe will be further promoted by TiN. These results are consistent with the observed complex nucleus and the increased EZR of Ingot B.

ACKNOWLEDGMENT

This work was supported by the National Natural Science Foundation of China [Project Grant No. 51374020].

REFERENCES

1. X.F. Shi, G.G. Cheng, and P. Zhao: *J. Univ. Sci. Technol. B.*, 2010, vol. 32, pp. 1277–81.
2. Y. Shan, X. Luo, X. Hu, and S. Liu: *J. Mater. Sci. Tech.*, 2011, vol. 27, pp. 352–58.
3. H. Tomari, K. Fujiwara, K. Shimogori, T. Fukuzuka, and M. Kanda: *Corros.*, 1982, vol. 38, pp. 283–94.
4. H. Abo and Y. Hosoi: *Corros. Eng.*, 1979, vol. 28, pp. 584–94.
5. T. Shibata: *Trans. Iron Steel Inst. Jpn.*, 1983, vol. 23, pp. 785–88.
6. J.K. Kim, Y.H. Kim, J.S. Lee, and K.Y. Kim: *Corros. Sci.*, 2010, vol. 52, pp. 1847–52.
7. J.K. Kim, Y.H. Kim, S.H. Uhm, J.S. Lee, and K.Y. Kim: *Corros. Sci.*, 2009, vol. 51, pp. 2716–23.
8. J.K. Kim, B. Lee, B.H. Lee, Y.H. Kim, and K.Y. Kim: *Scripta Mater.*, 2009, vol. 61, pp. 1133–36.
9. J.D. Fritz and I.A. Franson: *Mater. Sel. Des.*, 1997, vol. 36, pp. 57–61.
10. K. Suzuki, S. Asami, and K. Suzuki: *Tetsu-to-Hagane*, 1977, vol. 63, pp. 855–64.
11. E. Pouillard and B. Osdoit: *Rev. Metall.*, 1966, vol. 63, pp. 679–90.
12. R.N. Wright: *Metall. Trans.*, 1972, vol. 3, pp. 83–91.
13. H. Chao: *Metall. Trans.*, 1973, vol. 4, pp. 1183–86.
14. M.Y. Huh and O. Engler: *Mater. Sci. Eng. A*, 2001, vol. 308, pp. 74–87.
15. H. Shin, J. An, S. Park, and D. Lee: *Acta Mater.*, 2003, vol. 51, pp. 4693–4706.
16. O. Engler, M.-Y. Huh, and C.N. Tome: *Metall. Mater. Trans. A*, 2005, vol. 36A, pp. 3127–39.
17. H.J. Bong, F. Barlat, M.G. Lee, and D.C. Ahn: *Int. J. Mech. Sci.*, 2012, vol. 64, pp. 1–10.
18. X. Ma, J. Zhao, W. Du, X. Zhang, and Z. Jiang: *Mater. Charact.*, 2018, vol. 137, pp. 201–11.
19. Y. Bai, T. He, and Y. Liu: *Mater. Charact.*, 2018, vol. 137, pp. 142–50.
20. C.-Z. Lu, Z. Fang, and J.-Y. Li: *Mater. Charact.*, 2018, vol. 135, pp. 257–64.
21. K. Kawahara: *J. Japan Inst. Metals*, 1974, vol. 38, pp. 440–46.
22. Y. Itoh, T. Okajima, and K. Tashiro: *Tetsu-to-Hagane*, 1980, vol. 66, pp. 1093–1102.
23. H. Takeuchi, H. Mori, Y. Ikehara, T. Komano, and T. Yanai: *Tetsu-to-Hagane*, 1980, vol. 66, pp. 638–46.
24. Y. Itoh, S. Takao, T. Okajima, and K. Tashiro: *Tetsu-to-Hagane*, 1980, vol. 66, pp. 710–16.
25. Y. Itoh, T. Okajima, H. Maede, and K. Tashiro: *Tetsu-to-Hagane*, 1981, vol. 67, pp. 946–53.
26. N. Tsuji, K. Tsuzaki, and T. Maki: *ISIJ Int.*, 1993, vol. 33, pp. 783–92.
27. S. Park, K. Kim, Y. Lee, and C. Park: *ISIJ Int.*, 2002, vol. 42, pp. 100–05.
28. J. Hamada, Y. Matsumoto, F. Fudanoki, and S. Maeda: *ISIJ Int.*, 2003, vol. 43, pp. 1989–98.
29. C. Shi, G. Cheng, Z. Li, and P. Zhao: *J. Iron Steel Res. Int.*, 2008, vol. 15, pp. 57–60.
30. J.H. Park: *Calphad*, 2011, vol. 35, pp. 455–62.
31. A. Ito, H. Suito, and R. Inoue: *ISIJ Int.*, 2012, vol. 52, pp. 1196–1205.
32. J.C. Kim, J.J. Kim, J.Y. Choi, J.H. Choi, and S.K. Kim: *La Metall. Ital.*, 2009, vol. 101, pp. 43–48.
33. B.L. Bramfitt: *Metall. Trans.*, 1970, vol. 1, pp. 1987–95.
34. C. Shi: Univ. Sci. Technol. B, Beijing, Master Thesis, 2004.
35. H. Fujimura, S. Tsuge, Y. Komizo, and T. Nishizawa: *Tetsu-to-Hagane*, 2001, vol. 87, pp. 707–12.
36. S. Fukumoto, K. Kimura, and A. Takahashi: *Tetsu-to-Hagane*, 2012, vol. 98, pp. 351–57.
37. K. Kimura, S. Fukumoto, G. Shigesato, and A. Takahashi: *ISIJ Int.*, 2013, vol. 53, pp. 2167–75.
38. X. Shi, G. Cheng, and P. Zhao: *J. Univ. Sci. Technol. B.*, 2010, vol. 32, pp. 1277–81.
39. X. Shi: Univ. Sci. Technol. B., Beijing, Doctoral Thesis, 2010.
40. H. Inoue and T. Koseki: *Acta Mater.*, 2017, vol. 124, pp. 430–36.
41. J.Y. Kim, N.R. Oh, Y.H. Oh, Y.T. Cho, W.B. Lee, S.K. Kim, and H.U. Hong: *Mater. Charact.*, 2017, vol. 132, pp. 348–53.
42. J. Fu, W. Qiu, Q. Nie, and Y. Wu: *J. Alloys Compd.*, 2017, vol. 699, pp. 938–46.

43. J.S. Park, D.H. Kim, and J.H. Park: *J. Alloys Compd.*, 2017, vol. 695, pp. 476–81.
44. M. Gäumann, R. Trivedi, and W. Kurz: *Mater. Sci. Eng. A*, 1997, vols. 226–28, pp. 763–69.
45. R. Trivedi and W. Kurz: *Acta Metall.*, 1986, vol. 34, pp. 823–30.
46. Y. Hou, S. Li, and G. Cheng: *Metall. Mater. Trans. A*, 2018, vol. 49A, pp. 5445–57.
47. M.C. Flemings: *Solidification Processing*, McGraw-Hill, New York, 1974.
48. W. Kurz and D.J. Fisher: *Fundamentals of Solidification*, Trans. Tech. Publications, Switzerland, 1998.
49. J.S. Park and J.H. Park: *Steel Res. Int.*, 2014, vol. 85, pp. 1303–09.
50. S.K. Kim, H. Suito, and R. Inoue: *ISIJ Int.*, 2012, vol. 52, pp. 1935–44.
51. C. Ma and G.R. Rossman: *Am. Miner.*, 2009, vol. 94, pp. 841–44.
52. Y. Chen and J. Mao: *J. Mater. SCI-Mater. El.*, 2014, vol. 25, pp. 1284–88.
53. W. Spengler, R. Kaiser, A.N. Christensen, and G. Müller-Vogt: *Phys. Rev. B*, 1978, vol. 17, pp. 1095–1101.
54. J.H. Park: *Metall. Mater. Trans. B*, 2013, vol. 44B, pp. 938–47.
55. P. Fan and W.D. Cho: *Metall. Mater. Trans. B*, 2007, vol. 38B, pp. 713–17.
56. H. Sakai and H. Suito: *ISIJ Int.*, 1996, vol. 36, pp. 143–49.
57. K. Nomura, B. Ozturk, and R.J. Fruehan: *Metall. Mater. Trans. B*, 1991, vol. 22B, pp. 783–90.
58. S.-W. Cho and H. Suito: *Metall. Mater. Trans. B*, 1994, vol. 25B, pp. 5–13.
59. J.C. Villafuerte, H.W. Kerr, and S.A. David: *Mater. Sci. Eng. A*, 1995, vol. 194, pp. 187–91.
60. G.V. Pervushin and H. Suito: *ISIJ Int.*, 2001, vol. 41, pp. 748–56.
61. G.H. Gulliver: *J. Inst. Met.*, 1913, vol. 9, pp. 120–57.
62. E. Scheil: *Zeitschrift für Metallkunde*, 1942, vol. 34, pp. 70–72.
63. H. Goto, K. Miyazawa, W. Yamada, and K. Tanaka: *ISIJ Int.*, 1995, vol. 35, pp. 708–14.
64. J.S. Park, C. Lee, and J.H. Park: *Metall. Mater. Trans. B*, 2012, vol. 43B, pp. 1550–64.
65. N. Pan, B. Song, Q. Zhai, and B. Wen: *J. Univ. Sci. Technol. B.*, 2010, vol. 32, pp. 179–82.

Publisher's Note Springer Nature remains neutral with regard to jurisdictional claims in published maps and institutional affiliations.